ACS APPLIED MATERIALS & INTERFACES

Research Article

www.acsami.org

Bulk and Surface Excitons in Alloyed and Phase-Separated ZnO–MgO Particulate Systems

Huanjun Zhang,[†,‡] Amir R. Gheisi,[†,§] Andreas Sternig,[§] Knut Müller,[⊥] Marco Schowalter,[⊥] Andreas Rosenauer,[⊥] Oliver Diwald,[*,§] and Lutz Mädler[*,‡]

[‡]Foundation Institute of Materials Science (IWT), Department of Production Engineering, University of Bremen, Badgasteinerstraße 3, 28359 Bremen, Germany

[§]Institute of Particle Technology, Friedrich–Alexander University, Erlangen–Nürnberg, Cauerstraße 4, 91058 Erlangen, Germany

[⊥]Institute of Solid State Physics, University of Bremen, Otto–Hahn–Allee 1, 28359 Bremen, Germany

Supporting Information

ABSTRACT: The rational design of composite nanoparticles with desired optical and electronic properties requires the detailed analysis of surface and bulk contributions to the respective overall function. We use flame spray pyrolysis (FSP) to generate nanoparticles of the ternary Zn–Mg–O system the compositions of which range from solid solutions of Zn^{2+} ions in periclase MgO to phase separated particle mixtures which consist of periclase (cubic) MgO and wurtzite (hexagonal) ZnO phases. The structure and composition of the composite $Zn_xMg_{1-x}O$ ($0 \le x \le 0.3$) particles are investigated using X-ray diffraction and high-resolution transmission electron microscopy, whereas UV diffuse reflectance and photoluminescence (PL) spectroscopy are used for the investigation of their optical properties. Vacuum annealing has been carried out to track the effects of stepwise elimination of surface adsorbates on the photoexcitation and PL emission properties. We demonstrate that for $Zn_{0.1}Mg_{0.9}O$ particles, the admixed ZnO suppresses the MgO specific surface excitons and produces a PL emission band at 470 nm. Although gaseous oxygen partially reduces the emission intensity of hydroxylated particles, it leads to entire quenching in completely dehydroxylated samples after vacuum annealing at 1173 K. Consequently, surface hydroxyls at the solid–gas interface play a significant role as protecting groups against the PL-quenching effects of O_2. The obtained results are relevant for the characterization of ZnO-based devices as well as for other metal oxide materials where the impact of the surface composition on the photoelectronic properties is usually neglected.

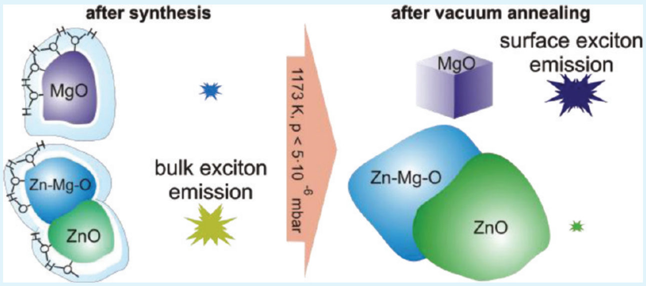

KEYWORDS: *composite, aerosol, nanoparticle, doping, photoluminescence, photoelectronic*

INTRODUCTION

Composite nanoparticle systems are increasingly important for applications that rely on the controlled synergistic combination of single-component properties. To understand their property changes during synthesis, processing and under operation conditions in a device, the rational development of functional nanomaterials requires careful evaluation of the physical properties in the bulk and at the interfaces. Magnesium oxide and zinc oxide are very distinct materials with regard to their crystallographic and electronic structures. The photoexcitation of highly dispersed MgO and other alkaline earth oxides, for instance, leads to the generation of surface excitons that depend on the chemical composition of the particle surface, and therefore, can be employed as surface probes.[1,2] On the other hand, the semiconductor ZnO (bandgap $E_{bg} \approx 3.4$ eV) with its bulk luminescence properties has attracted great attention because of its potential for UV light-emitting diodes (LEDs), lasers and various other optoelectronic applications.[3−5] Moreover, admixing ZnO into MgO ($E_{bg} \approx 7.6$ eV) provides means for engineering the bulk electronic structure.[6−8] Most of related studies on such particle systems are dedicated to ZnO wurtzite structures with small amounts of MgO admixed, whereas considerably fewer studies report periclase MgO doped with ZnO. A promising aspect of such composites is related to the metastable cubic ZnO phase[9] that is expected to be compatible for *p*-type doping.[10] Different synthesis methods including the sequential implantation of Zn^+ and O^+ ions in single-crystalline MgO,[11] the calcination of polymer/metal salt complexes[12] or reactive electron beam evaporation[13] have been employed for the generation of cubic ZnO structures. But detailed synthesis and characterization studies on powders of well–dispersed $Zn_xMg_{1-x}O$ nanocrystals are scarce, because of the lack of appropriate preparation techniques and reliable surface

Received: February 1, 2012
Accepted: April 24, 2012
Published: April 24, 2012

characterization approaches, which are crucial to understand the material properties related to the gas−solid interface.

In a previous work we have shown that monocrystalline $Zn_xMg_{1-x}O$ (x denotes the molar ratio between Zn and (Zn+Mg)) nanocubes of exceptional regular cubic shape and edge lengths below 25 nm can be produced by chemical vapor synthesis (CVS).[14] In line with ab initio calculations, the annealing induced Zn^{2+} segregation into low coordinated surface sites of MgO nanocubes was tracked with UV diffuse reflectance, FT−IR and PL spectroscopy. We observed completely new PL emission features which were perfectly quenched upon exposure to gaseous oxygen, demonstrating that corresponding excitation and subsequent radiative deactivation processes are directly linked to excitons formed at the surface of the composite nanocubes. Higher ZnO loadings with concentrations above the solubility limit of Zn^{2+} in MgO are expected to lead to particle systems where annealing induced phase separation[15] would generate highly dispersed ZnO deposits in contact with thermally stable MgO-based support particles. Such an approach would provide particulate model systems where a systematic comparison between photoexcited surface states on MgO as well as electronic transitions induced in ZnO can provide substantial insights into stability and surface electronic structure of pure and composite ZnO nanomaterials. However, as a major shortcoming of the direct combustion of Zn and Mg vapors (CVS), an upper concentration limit of approximately 12 at % ZnO results from the fact that during the combustion process Zn vapor cools down the flame and in this way prevents the reproducible metal combustion over longer periods of time. For the realization of composite ZnO/MgO systems with higher Zn^{2+} concentrations, longer production times and higher yields, Zn vapor needs to be added in a more effective and controllable way to the combustion zone. As an alternative approach the versatile flame spray pyrolysis process can be scaled up to production rates of kg h^{-1}.[16−18] ZnO and MgO nanoparticles were successfully produced with flame spray pyrolysis in the past. However, there exists only one report on the flame spray synthesis of $Zn_xMg_{1-x}O$ nanoparticles which focuses on Mg−doping of ZnO and is limited to the description of basic powder properties.[19]

This paper has three major objectives: first, we want to explore the potential of flame spray pyrolysis (FSP) with respect to the generation of particles of the ternary Zn−Mg−O system the compositions of which range from solid solutions of Zn^{2+} ions in periclase MgO[14] to mixtures where phase separation into a MgO rich periclase and a ZnO rich wurtzite phase occurs. Second, we want to study the influence of annealing induced surface dehydroxylation and removal of surface contaminants on the surface electronic structure of ZnO based particle systems. As shown in previous papers[1,2] the in depth characterization of interfacial effects requires treatment and measurements of nanoparticle powders in defined gas atmospheres such as high vacuum ($p < 1 \times 10^{-5}$ mbar) or oxygen atmosphere. The third objective of this study aims at the identification of potential synergistic effects between ZnO and MgO that originate from surface and bulk doping, as well as from segregation and phase separation effects.

EXPERIMENTAL SECTION

Chemicals. Anhydrous magnesium(II) acetylacetonate (Strem Chemicals, 98%) and zinc(II) naphthenate (Strem Chemicals, 65% in mineral spirits in naphthenic acid) were used as received as the source of Mg and Zn, respectively, for the flame synthesis of Zn−doped MgO. A mixture of xylene (BDH, ≥ 98.5%) and ethanol absolute (RDH, ≥ 99.8%) was used as solvents for preparing the precursor solutions. To increase the Mg(II) concentration in the precursor solutions, 2-ethylhexanoic acid (RDH, ≥ 99%) was used to dissolve the Mg(II) salt.

FSP Synthesis. Zinc-doped MgO ($Zn_xMg_{1-x}O$) powders were synthesized in a flame spray reactor. Detailed description of the setup can be found elsewhere.[20] For the preparation of the precursor solutions, 56.8 g of Mg(II) acetylacetonate was dissolved in a mixture of 2−ethylhexanoic acid (167.2 mL), ethanol absolute (100.0 mL) and certain amount of xylene, to make a final volume of 500.0 mL, corresponding to an Mg(II) concentration of 0.5 mol/L. The Zn(II) solution (0.5 mol/L) was made by diluting 81.7 g of Zn(II) naphthenate (in naphthenic acid as received) with xylene to a final volume of 250.0 mL. The Mg(II) and Zn(II) solutions were mixed at chosen volume ratio to achieve the desired Zn(II) doping levels while keeping the total metal concentration of 0.5 mol/L in the precursor solutions.

During flame spray pyrolysis experiments, the mixed precursor solution was fed by a syringe pump (KD Scientific) at a fixed flow rate of 5.0 mL/min. The liquid was dispersed into fine droplets by O_2 gas (5.0 L/min, 1.5 bar) at the spray nozzle exit. The spray was ignited by a CH_4/O_2 (1.5 and 3.2 L/min, respectively) supporting flame to form a self−sustained flame. The flow rates of all gases were controlled by calibrated mass flow controllers (Bronkhorst High-Tech). The generated $Zn_xMg_{1-x}O$ particles were directed by a vacuum pump and collected on a water-cooled glass fiber filter (Whatman GF−6) placed 450 mm above the nozzle. After being collected from the filter surface, the powders were sieved to remove the glass fibers.

XRD, N_2 Physisorption, HRTEM, EDS, and HAADF−STEM Characterizations. Powder X-ray diffraction analysis was carried out on a PANalytical X'pert diffractometer with Cu Kα radiation source. Silicon zero−background plates were used as the sample holder. The scanning program covers a 2θ range between 15 and 140° at a step size of 0.03°. Rietveld refinements of the XRD patterns were conducted using commercial refinement software (Bruker AXS Topas 4.2) to analyze the crystal structure and quantify the phase concentration of the products. The Brunauer−Emmett−Teller specific surface area (BET SSA) of the as−synthesized $Zn_xMg_{1-x}O$ powder was measured through N_2 physisoprtion at liquid nitrogen temperature using a Quantachrome Nova analyzer. The samples were degassed at 473 K for 4 h before dosing with N_2.

High-resolution transmission electron microscopy (HRTEM) was conducted on an FEI Titan 80/300 electron microscope operated at 300 kV to investigate the morphology and the microscopic elemental composition of the as−synthesized powders. In particular, energy-dispersive X-ray spectra (EDS) were collected from the samples in the scanning transmission electron microscopy (STEM) mode, in which Z-contrast imaging was performed with a high-angle annular dark-field (HAADF) detector. The EDS spectra were used to analyze the spatial distribution of Mg, Zn, and O elements on the length scale of a few hundred nanometers. Electron diffraction was also performed to study the crystal structure of the samples. The TEM samples were prepared by dispersing the as-synthesized particles in isopropanol using an ultrasonic bath. Several drops of the suspension were dropped onto carbon-coated copper grids, which were then subjected to vacuum storage before TEM experiments.

Vacuum Annealing and Optical Investigations. To investigate the dependence of their optical properties on the surrounding atmosphere, we transferred the powder samples into quartz glass cells, within which thermal activation of the powders and spectroscopic measurements were performed in high vacuum (at base pressure $<5 \times 10^{-6}$ mbar unless otherwise specified). A typical procedure for dehydration, dehydroxylation and the removal of carbon−based surface contaminants is as follows: the as-synthesized powders are heated to 1123 K in high vacuum at a rate of 5 K min^{-1} and are then brought into contact with 10 mbar O_2 at this temperature. Subsequently, the sample−cell temperature is raised to 1173 K and is kept at this temperature for 30 min before being cooled down to room temperature.

UV diffuse reflectance spectra were acquired in the presence of 10 mbar of O_2 using a Perkin-Elmer Lambda 950 spectrophotometer equipped with an integrating sphere and then converted to absorption spectra using the Kubelka−Munk transformation. PL spectra were measured on a Horiba Jobin Yvon Fluorolog−3 system (FL3−22) using a cw 450 W xenon arc lamp for excitation. The spectrometer is equipped with a double monochromator in emission and excitation to guarantee optimal stray-light rejection. After vacuum annealing, the processed powders were further characterized by N_2 physisorption and TEM.

■ RESULTS AND DISCUSSION

Characterization Results. *Powder XRD.* The powder XRD patterns of the as-synthesized $Zn_xMg_{1-x}O$ samples are shown in Figure 1. The XRD pattern of the as-synthesized MgO shows a periclase structure with the most intense diffraction peak (002) at 42.96°. The relative positions of other weaker peaks of this sample also match the periclase space group (fm$\bar{3}$m), although with some small shifts in 2θ. Rietveld refinement results in an average crystallite size of 9.9 nm (Table 1). With Zn doping at a loading of 10% ($x = 0.1$), the XRD pattern is rather similar to that of pure MgO. No signature of other crystalline phases including wurtzite ZnO can be identified, indicating a solid solution of Mg−Zn−O with Zn being well blended into the lattice structure of periclase MgO during the flame spray pyrolysis process. Rietveld refinement results in an average crystallite size of 10.5 nm, slightly larger than that of the pure MgO sample.

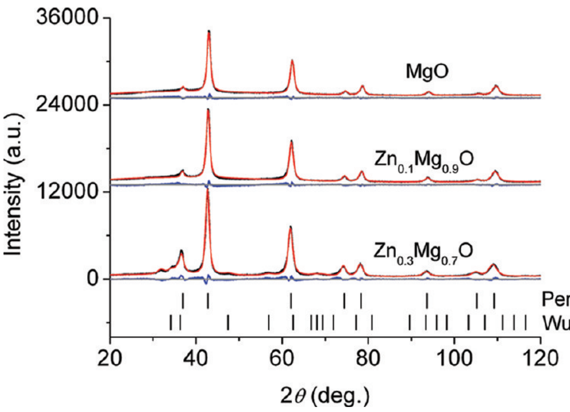

Figure 1. Powder XRD patterns and Rietveld refinement results from FSP−made $Zn_xMg_{1-x}O$ samples. The raw XRD data, the refined patterns and their differences are presented in black, red and blue colors, respectively. Diffraction peaks for cubic MgO and hexagonal ZnO are also shown as bars to indicate their 2θ positions.

When the Zn loading is further increased ($x = 0.3$), diffraction peaks start to emerge at 31.93, 34.14, 47.44, 56.89, and 68.04°, corresponding to (010), (002), (012), (110), and (112) diffractions of wurtzite ZnO. The peak at 36.66° should be contributed by both ZnO (011) and MgO (111) diffractions, if we compare the intensity here with those at $x = 1$ and $x = 0.9$. These results show that at a high Zn loading (30%), a certain amount of ZnO is phase-separated from periclase MgO to form wurtzite structures. Rietveld refinement gives an average periclase crystallite size of 10.4 nm and wurtzite crystallite size of 9.8 nm. Quantitatively, a wurtzite concentration of 5.9% in weight percentage was estimated. Therefore, the majority of Zn is blended into the periclase MgO lattices. The nominal formula for this solid solution is calculated as $Zn_{0.27}Mg_{0.73}O$, corresponding to a wurtzite-to-periclase molar ratio of 1:25 (calculation details in the Supporting Information).

It is also observed that as the Zn loading increases, the diffraction peaks of the periclase phase slightly shift to the lower angle. Based on Bragg's law ($n\lambda = 2d \sin \theta$), the d-spacing and hence the lattice constant are expected to increase. As shown in Table 1, the a value increases from 4.22 Å for pure MgO to 4.24 Å for $Zn_{0.27}Mg_{0.73}O$ accordingly. This lattice expansion can be explained by the slightly larger ionic radius of Zn^{2+} (0.74 Å) than that of Mg^{2+} (0.72 Å) in the periclase phase.[21] Such a trend further supports that Zn^{2+} has been incorporated into the Mg^{2+} sites in the cubic lattice as the Zn loading increases, leading to a monotonous, although small, expansion of the unit cell. On the other hand, the lattice constants of the segregated wurtzite phase at $x = 0.3$ were also found to differ slightly from those of pure FSP−synthesized ZnO (XRD and Rietveld refinement data not shown here). The lattice constants in the a- and c-axis of the separated wurtzite phase are 3.24 and 5.22 Å, respectively, indicating a slight compression in the a-axis and expansion in the c−axis, as compared to the refined 3.25 Å (a) and 5.21 Å (c) of the pure ZnO sample. Such a change is consistent with the reported trend for Mg-doped ZnO thin films.[22,23]

Although the wurtzite-structured Mg−Zn−O solid solutions (mostly epitaxially grown thin films) have been actively investigated during the past decade,[22,24−26] their counterparts, i.e., the cubic-structured solid solutions, have been much less addressed, especially in the powder or particle form. The solubility limit of ZnO in the FSP-made samples measured here, 27% (molar percentage), closely matches that predicted by MgO−ZnO phase diagram as reported by Segnit and Holland.[10] In their work, a solubility limit of 28.8% for ZnO at 1000 °C in the cubic Mg−Zn−O solid solution was estimated.

N_2 Physisorption. The results of N_2 physisorption (7-point BET) analysis on the FSP−made $Zn_xMg_{1-x}O$ powders are also

Table 1. Summary of the Results from Powder XRD and N_2 Physisorption Analyses on $Zn_xMg_{1-x}O$

	after synthesis					after vacuum annealing			
	d_{XRD} (nm)[a]					d_{XRD} (nm)[a]			
samples	MgO phase	ZnO phase	SSA (m^2/g)	d_{BET}[b] (nm)	a_{MgO}[a] (Å)	MgO phase	ZnO phase	SSA (m^2/g)	d_{BET}[b] (nm)
MgO	9.9	N/A[c]	190	8.9	4.22	10.6	N/A[c]	150	11.2
$Zn_{0.1}Mg_{0.9}O$	10.5	N/A[c]	172	8.9	4.22	11.9	N/A[c]	110	13.9
$Zn_{0.3}Mg_{0.7}O$	10.4	9.8	143	9.1	4.24	49.1	54.0	17	76.1

[a] Calculated from Rietveld refinement of the powder XRD patterns. [b] Calculated using the formula $d_{BET} = 6/(\rho SSA)$, where ρ is the molar-average density of the samples based on the densities of cubic $Zn_xMg_{1-x}O$ and hexagonal ZnO, g m^{-3}. [c] The ZnO crystallite sizes are not calculated because no diffraction peaks corresponding to the wurtzite phase were observed from the powder XRD profiles.

shown in Table 1. As the Zn loading increases from 0 to 30% (molar), the specific surface area decreases from 190 to 143 m^2/g. On the basis of the formula $d_{BET} = 6/(\rho SSA)$, the average particle size is estimated to be 8.9, 8.9, and 9.1 nm for 0, 10, and 30% Zn-doped MgO samples, respectively. These results indicate that introducing Zn into MgO does not significantly change the average particle size. The particle sizes estimated by N_2 physisorption here are close to those calculated from Rietveld refinement, indicating single−crystalline particles formed.

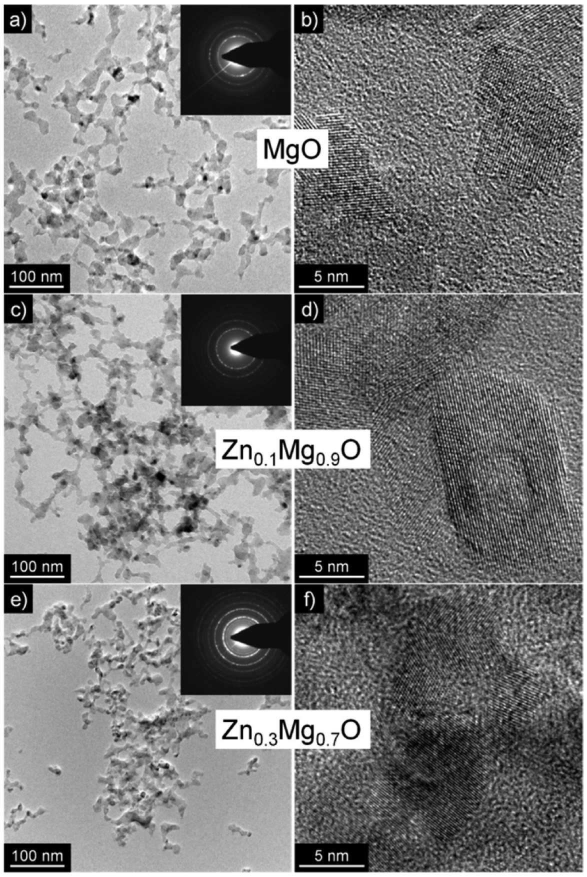

Figure 2. Results of TEM characterization on the $Zn_xMg_{1-x}O$ samples. The insets in a, c, and e show the electron diffraction patterns of each sample.

TEM/Electron Diffraction. The morphology of the as-synthesized $Zn_xMg_{1-x}O$ particles was studied using transmission electron microscopy, as shown in Figure 2. The low—resolution TEM images (Figure 2a, c, e) show comparable particle sizes at various Zn loadings. Individual particles are interconnected to form aggregates, which is a typical feature for flame-synthesized materials. HRTEM imaging (Figure 2b, d, f) reveals the highly crystalline nature of the as-synthesized particles, regardless of the Zn loading. Sharp edges of the single particles are visible with no evidence of an amorphous covering layer. The crystallite size in each sample is about 10 nm, which closely matches the results from Rietveld refinement of the XRD patterns and the BET analysis. The observation again suggests that these nanoparticles are individually single−crystalline. Electron diffraction probing (insets in Figure 2a, c, e) shows for a Zn loading of 10% a similar set of rings (Figure 2g, h), whereas for the 30% Zn loading, new rings occur belonging to the diffraction patterns of wurtzite ZnO. The electron diffraction patterns corroborate the powder XRD results.

EDS and HAADF−STEM. Energy-dispersive X-ray spectroscopy in TEM mode was used to analyze the chemical compositions of the $Zn_xMg_{1-x}O$ particle aggregates. The Zn loadings detected by conventional EDS probing are 9.5% and 25.6% for the nominal loadings of 10 and 30%, respectively, suggesting a good fidelity of the product composition to the precursor solution design. Furthermore, by conducting EDS analysis under the HAADF−STEM mode, we expect to investigate the distribution of the Mg, Zn and O elements on the submicrometer length scale while retaining a resolution of a few nanometers, in order to identify the events of ZnO phase separation. Using this mode, as the electron beam scans the sample, the EDS spectra were collected at a series of locations and the total intensity of the collected X-ray intensity is decomposed according to the Mg, Zn and O energy windows to give element-specific photon intensities along the scanned path on the length scale of hundreds of nanometers. We combine EDS with HAADF−STEM imaging because it is difficult, on this length scale, to precisely reveal the spatial distribution of different elements by Z-contrast imaging alone, considering the powder nature of the samples and their uneven thickness. The results are shown in Figure 3.

For the pure MgO sample (Figure 3a, b), the signal intensity of Mg goes in phase with that of O on a length scale of 80 nm.

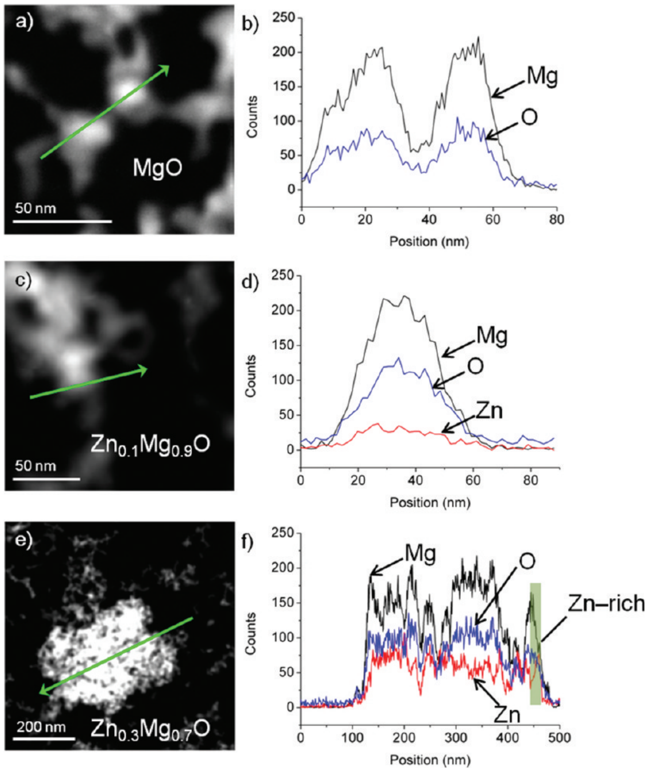

Figure 3. Results of EDS analysis under the STEM−HAADF mode. (a, c, e) STEM−HAADF images of MgO, $Zn_{0.1}Mg_{0.9}O$, and $Zn_{0.3}Mg_{0.7}O$, respectively; (b, d, f) Spatial variation of the EDS signal intensities of different elements in MgO, $Zn_{0.1}Mg_{0.9}O$, and $Zn_{0.3}Mg_{0.7}O$, respectively. For each sample, a typical EDS spectrum was recorded first and used to define the energy windows for different elements, which were then used to decompose the total counts of photons to element-specific intensities.

At 10% Zn loading (Figure 3c, d), the change of the intensity in the Mg signal is still in phase with that of the O signal; in addition, the measured Zn signal is also in phase with those of Mg and O, suggesting a homogeneous blending of Zn into the MgO lattice. Such results of microscopic compositional analysis are consistent with the XRD analysis results, which show no noticeable phase separation of ZnO at 10% of Zn. When the Zn loading increases to 30%, the patterns of the EDS signals bear more structures, as shown in Figure 3e, f. The scanning distance is about 500 nm. In contrast to the synchronized trends in Figure 3b, d, in certain regions in Figure 3f the Mg and Zn signals show out−of−phase trends of variation. For instance, there are regions where the intensity of Mg drops significantly while the Zn intensity keeps almost constant; in certain other regions, the intensities of the Mg and Zn signals vary in opposite directions. Such information indicates that at 30% Zn loading, the distribution of Zn within the MgO matrix is inhomogeneous. The results are in good agreement with the powder XRD data from which ZnO phase separation is identified. Furthermore, it should be within the relatively Zn−abundant regions (e.g., the rightmost part of the highlighted "Zn-rich" region in Figure 3f) that the segregation of wurtzite ZnO is expected to occur. Note that the trends found in Figure 3 are typical and the elemental distribution results are representative of all samples.

Vacuum Annealing, Structural Changes, and Optical Properties. In comparison to the UV diffuse reflectance spectra of the MgO sample (Figure 4a), the spectra of the as-synthesized $Zn_{0.1}Mg_{0.9}O$ and $Zn_{0.3}Mg_{0.7}O$ samples show Zn^{2+}-induced changes in the absorption properties (Figure 4b, c, respectively). These changes are either characterized by a red−shifted absorption band ($Zn_{0.1}Mg_{0.9}O$, Figure 4b) or an absorption threshold at 3.4 eV which is consistent with the band gap of ZnO (Figure 4c).[3] This latter observation of the $Zn_{0.3}Mg_{0.7}O$ sample is supported by the XRD data (Figure 1, Table 1) and EDS analysis under the STEM mode (Figure 3e, f). Phase separation into a MgO−rich periclase phase and a ZnO−rich wurtzite phase should have occurred during the flame synthesis where the particles are exposed to flame temperatures of above 2000 K. While vacuum annealing at 1173 K does not affect the absorption edge of $Zn_{0.3}Mg_{0.7}O$ (gray and black curves in Figure 4c), the absorption−edge shift observed for the $Zn_{0.1}Mg_{0.9}O$ sample (Figure 4b) points to a modification of the electronic structure that originates from the annealing-induced Zn^{2+} segregation into the particle surface.[14]

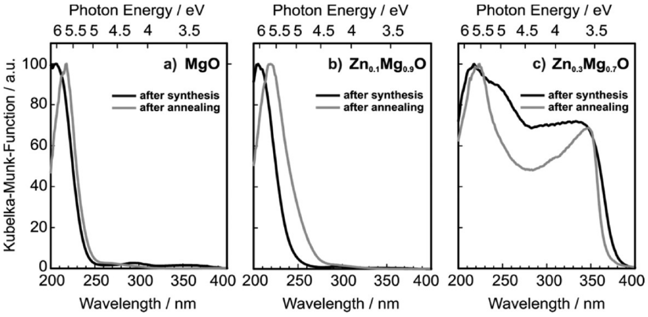

Figure 4. UV diffuse reflectance spectra of (a) MgO, (b) $Zn_{0.1}Mg_{0.9}O$, and (c) $Zn_{0.3}Mg_{0.7}O$ before (black) and after (gray) vacuum annealing at 1173 K for 30 min. The spectra were acquired at room temperature and in the presence of 10 mbar O_2.

For a clearer comparison, the UV diffuse reflectance spectra of the annealed powders are plotted in Figure 5a in conjunction with their TEM images shown in Figure 5b−d. Vacuum annealing of MgO leads to the optical absorption behavior (Figure 5a) and the cubic shape (Figure 5b) that are characteristic of MgO nanocubes with an average edge length of 10 nm. Both observations are consistent with the properties of CVS−grown MgO powders.[27,28] The sharpness of the cubic morphology is not preserved upon admixing of Zn^{2+} (Figure 5c, d).

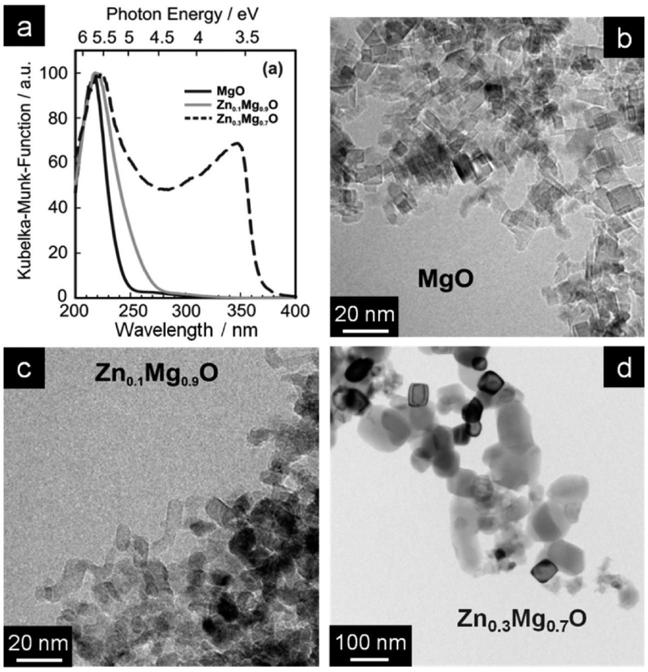

Figure 5. (a) UV diffuse reflectance spectra and (b−d) TEM images of MgO, $Zn_{0.1}Mg_{0.9}O$ and $Zn_{0.3}Mg_{0.7}O$ nanoparticles after vacuum annealing at 1173 K for 30 min (the spectra were acquired at room temperature in the presence of 10 mbar O_2).

Powder XRD analysis and Rietveld refinement results show that vacuum annealing causes different degrees of crystallite−size increase in periclase and wurtzite domains (Table 1). The average crystallite sizes of MgO and $Zn_{0.1}Mg_{0.9}O$ (both possessing only the periclase phase) increase by 7% and 14%, respectively. In the case of $Zn_{0.3}Mg_{0.7}O$, the crystallite size of the periclase domain grows by a factor of 4.7, whereas the crystallite size of the wurtzite phase increases by a factor of 5.5. TEM imaging results, as shown in Figure 5d and S1 (Supporting Information), are in good agreement with the crystallite sizes estimated by XRD analysis. Through high-resolution TEM studies on the vacuum annealed $Zn_{0.3}Mg_{0.7}O$ sample, we identified the phase-separated wurtzite domains with characteristic *d*-spacing of 0.247 nm of the (110) planes (see Figure S1b in the Supporting Information), which are in contrast to the periclase domains with the *d*-spacing of 0.212 nm of the (002) planes (see Figure S1d in the Supporting Information). These observations are consistent with the powder XRD patterns of the vacuum annealed $Zn_{0.3}Mg_{0.7}O$ sample (see Figure S1 in the Supporting Information). Such trends appear to indicate that Zn^{2+} ions inside the periclase lattice facilitate the crystallite growth, possibly by enhancing the mobility of the ions and/or ion vacancies. Meanwhile, such effects should favor the preferential segregation of Zn^{2+} ions into low coordinated surface sites.[14] Additional EDS analysis under the STEM−HAADF mode rules out the possibility of annealing−induced compositional changes such as the depletion of ZnO into the gas phase.

Based on the UV diffuse reflectance data (Figure 5a), we chose 270 and 340 nm as the excitation wavelengths for probing the PL emission properties of these powders.[27] For dehydroxylated MgO nanocubes, λ_{EXC} = 270 nm (4.6 eV) selectively excites the corner sites, whereas a wavelength of 340 nm (3.6 eV) should not produce photoexcited states in MgO. The photon energy of 3.6 eV; however, exceeds the band gap of ZnO and can be used to probe ZnO-specific electronic transitions. The as-synthesized MgO sample shows a broad PL emission feature with a maximum at 470 nm (Figure 6, black lines); the shape of the spectrum and the position of the maximum intensity are independent of the excitation wavelength. Admixing of 10% (atomic) Zn leads to a broadening of the emission feature and a blue shift of its maximum to 440 nm; again, the position of the maximum emission is independent of the excitation wavelength (Figure 6, gray lines). The PL emission intensity of both MgO and $Zn_{0.1}Mg_{0.9}O$ decreases upon changing the excitation wavelength from 270 to 340 nm. A narrow and so far unexplained emission feature at 680 nm (1.8 eV) is observed as well.

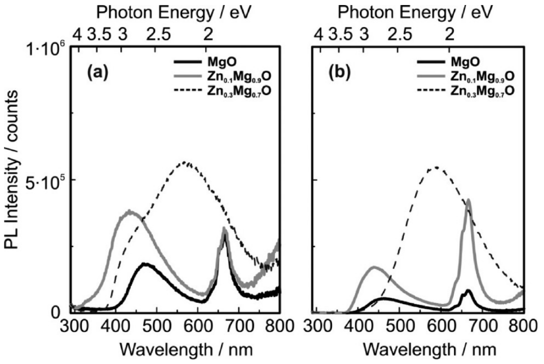

Figure 6. PL emission spectra of as-synthesized $Zn_xMg_{1-x}O$ nanoparticles acquired at <1 × 10^{-5} mbar and 298 K using excitation wavelengths of (a) 270 and (b) 340 nm, respectively. The emission spectra are not affected by the presence of 10 mbar O_2.

For $Zn_{0.3}Mg_{0.7}O$, both the shape of the PL emission spectrum and the position of its maximum depend on the excitation energy: with λ_{EXC} = 270 nm, an emission band at 560 nm with a shoulder at 430 nm suggests that the overall spectrum is composed of at least two contributions (Figure 6a, dashed line). An excitation wavelength of 340 nm produces an emission band at 590 nm (Figure 6b, dashed line), the intensity of which is comparable to the one being subjected to excitation with λ_{EXC} = 270 nm. All spectra in Figure 6 are insensitive to the presence of O_2 in the gas phase, i.e., no evidence is found for the energy transfer between the photoexcited particles and O_2 (previously established as a PL quencher[3,27]) from the gas phase.

To investigate the optical properties of the partially hydroxylated samples, the samples were subjected to annealing at 873 K prior to spectroscopic measurements. Previous studies on MgO nanoparticles have shown that vacuum annealing in combination with O_2 treatment is effective for the elimination of carbon based surface contaminants;[1,2] meanwhile, the concentration of hydrogen−bonded neighboring surface OH groups becomes negligibly low and only the bands pertaining to isolated surface hydroxyl groups remain.[29,30] As a result, the emission with a maximum at 560 nm which was previously observed on as−synthesized $Zn_{0.3}Mg_{0.7}O$ (Figure 6a) vanishes after being annealed at 873 K (Figure 7a and Figure S2 in the Supporting Information). Pure MgO powders show a strong surface dependent PL emission feature with a maximum at 470 nm (Figure 7). This band is quenched by O_2 from the gas phase, which is attributed to the protonated corner sites of partially hydroxylated MgO nanocubes.[29] This observation is in good agreement with the findings on CVS−grown MgO powders. Interestingly, Zn^{2+} admixed into MgO decreases the intensity of the PL emission. This effect is attributed to the annealing−induced segregation of Zn^{2+} ions into the edge and corner sites in the periclase domain, thus inducing the depletion of MgO-specific surface excitons.[14] As outlined in the Supporting Information (Figure S3) molecular oxygen does not entirely quench the PL emission band at 440 nm (2.8 eV). This is different from dehydroxylated particle surfaces and indicates that surface hydroxyls counteract energy transfer between photoexcited surface states and molecular oxygen.[31]

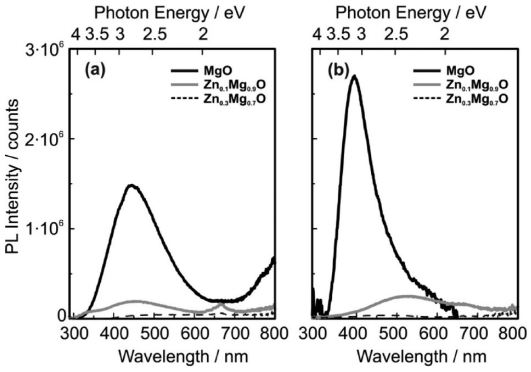

Figure 7. PL emission spectra of $Zn_xMg_{1-x}O$ nanoparticles after vacuum annealing at 873 (a) and 1173 K (b) (The dwell time at each temperature is 30 min; the spectra were acquired at <1 × 10^{-5} mbar and 298 K using λ_{EXC} = 270 nm). The PL emission of MgO is effectively quenched upon the addition of 10 mbar O_2 regardless of the annealing temperature. The PL emission of the $Zn_{0.1}Mg_{0.9}O$ sample is quenched by 10 mbar O_2 only after annealing at 1173 K.

The intensity loss of the green emission from the partially hydroxylated samples may have its origin in the annealing−induced annihilation of intrinsic bulk− or surface defects including the surface hydroxyls.[14,32−34] To address the latter possibility, we performed a control experiment by exposing the partially dehydroxylated $Zn_{0.3}Mg_{0.7}O$ sample to air for 24 h (see Figures S2 in the Supporting Information). Subsequently, after being pumped down to <1 × 10^{-6} mbar, the sample did not present a restoration of the PL emission observed before annealing. Apparently, simple surface hydroxylation via contact with moisture in the air is insufficient to restore the ZnO specific PL behavior. In case of the MgO samples, a PL emission at 2.7 eV (Figure 7a, black line) grows with the increase in annealing temperature while the band maximum shifts to 3.2 eV (Figure 7b, black line). This trend is consistent with the stepwise dehydroxylation of MgO nanocube surfaces upon generation of bare metal oxide particle surfaces where surface excitons can selectively form at corners and edges.[27]

Figure 8 schematically summarizes the observed trends in the photoelectronic properties of pure and Zn^{2+}-admixed MgO

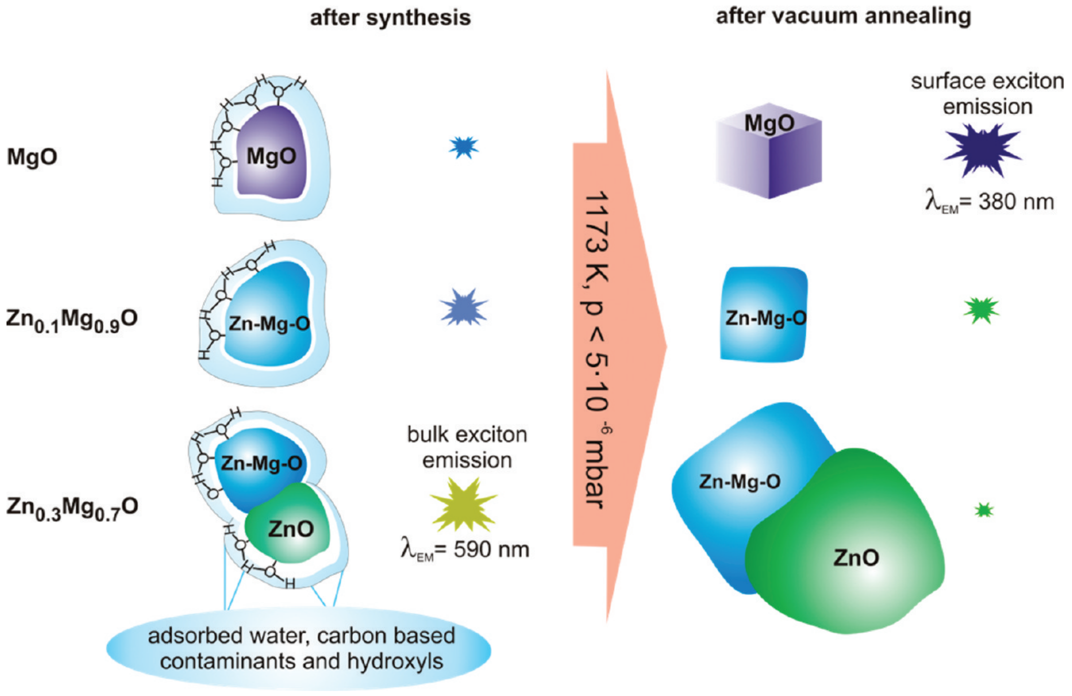

Figure 8. Schematic summary of the correlation between the surface states of the $Zn_xMg_{1-x}O$ particles and their PL emission properties. High-vacuum annealing leads to dehydroxylated MgO and Zn−Mg−O surfaces and morphological transformation of the particles. The size of the flashes qualitatively denotes the relative emission intensity that changes upon annealing.

particle systems as a result of annealing−induced surface cleaning. Starting with particles the surfaces of which are covered with adsorbates that are generated from the synthesis process (Figure 8, left), a PL emission at λ = 590 nm is observed only for the $Zn_{0.3}Mg_{0.7}O$ sample with a separated wurtzite phase (bottom of Figure 8). The corresponding excitation energy is below the threshold energy required to address low−coordinated surface sites on MgO particles. The independence of the PL emission on the surrounding gas atmosphere, in particular from molecular oxygen as a PL quencher, indicates that the underlying process corresponds to the radiative deactivation of bulk excitons.

Annealing at 873 K irreversibly extinguishes this ZnO specific PL feature and facilitates the formation of surface excitons on MgO particles (Figure 7). Moreover, such treatment not only removes carbon−based surface contaminants and eliminates the surface hydroxyls, but also favors ion mobility inside the lattice, therefore allowing for partial reorganization of the particles (Figure 8, right). While the MgO particles transform into cubes and essentially retain their high dispersion (Table 1), the admixing of Zn^{2+} ions reduces the thermal stability of the host component and leads to coarsened and morphologically less sharply defined particles. PL emission measurements clearly demonstrate that MgO specific surface excitons are strongly depleted by annealing-induced Zn^{2+} segregation into low-coordinated surface sites where surface excitons are formed and/or can radiatively deactivate. A new PL emission band with its maximum at λ = 520 nm is observed, which should originate from the Zn^{2+}-decorated MgO particle surface and is related to the chemical composition at the interface.

CONCLUSIONS

It has been demonstrated that flame spray pyrolysis is a valuable synthesis approach for the generation of ternary Zn−Mg−O nanoparticles. Powder XRD, Rietveld refinement and HRTEM−EDS collaboratively show that admixing 10% (atomic) of Zn into MgO leads to $Zn_{0.1}Mg_{0.9}O$ solid solutions, whereas admixing 30% of Zn gives rise to the phase separation into an MgO−rich periclase phase and a ZnO−rich wurtzite phase. Such structural differences critically affect the optical properties of the particles, as revealed by UV diffuse reflectance and PL emission measurements:

(1) The as-synthesized MgO nanoparticles show PL characteristics that are related to surface excitons associated with the corner sites of MgO nanocubes.[3,27]

(2) Phase-separated wurtzite ZnO inside the as-synthesized $Zn_{0.3}Mg_{0.7}O$ particles gives rise to a green PL emission at 590 nm. This process is not quenched by molecular oxygen in the gas phase. Removal of adsorbed water, hydroxyls, and possible carbonaceous contaminants by vacuum annealing and oxidation at 873 K leads to the extinction of this emission process. Subsequent surface hydroxylation via contact with air moisture does not restore this feature.

(3) Upon vacuum annealing, surface-segregation of Zn^{2+} ions causes depletion of MgO-specific PL emission. While exposure to gaseous O_2 partially reduces the PL emission intensity of hydroxylated $Zn_{0.1}Mg_{0.9}O$ particles, it quenches entirely the emission in dehydroxylated particles. Consequently, hydroxyls can be regarded as protecting groups against gaseous oxygen as a PL quencher at the solid−gas interface.

The present study clearly underlines the importance of sorting out the bulk and interface contributions to the overall optical performances of composite oxide nanomaterials that can be further engineered as components for optoelectronic applications.

ASSOCIATED CONTENT

Ⓢ Supporting Information

Details of calculating the chemical formula of the periclase-phase solid solution, TEM images showing the separated wurtzite and periclase domains in the vacuum-annealed $Zn_{0.3}Mg_{0.7}O$ sample, and details of the effects of exposure to air and oxygen atmosphere on the PL emission properties of the $Zn_xMg_{1-x}O$ samples. This material is available free of charge via the Internet at http://pubs.acs.org/.

■ AUTHOR INFORMATION

Corresponding Author

*E-mail: lmaedler@iwt.uni-bremen.de (L.M.); o.diwald@lfg.uni-erlangen.de (O.D.).

Author Contributions

[†]These authors contributed equally to this paper.

Notes

The authors declare no competing financial interest.

■ ACKNOWLEDGMENTS

The authors thank Deutsche Forschungsgemeinschaft (DFG) for funding this project within the Research Training Group 1375 "Nonmetallic Porous Structures for Physical-Chemical Functions". The support from the University of Bremen under the Initiative "Func-Band" is also gratefully acknowledged. The Erlangen group gratefully acknowledges the Austrian Funds zur Förderung der Wissenschaftlichen Forschung for grants FWF-P19848-N20 and FWF-PI312 (ERA Chemistry). A.R.G. is supported by grant FWF-PI312 (ERA Chemistry). This work also made use of the facilities of the Cluster of Excellence "Engineering of Advanced Materials" at the University of Erlangen−Nuremberg.

■ REFERENCES

(1) Sternig, A.; Stankic, S.; Mueller, M.; Bernardi, J.; Knoezinger, E.; Diwald, O. *Adv. Mater.* **2008**, *20*, 4840.

(2) Spoto, G.; Gribov, E. N.; Ricchiardi, G.; Damin, A.; Scarano, D.; Bordiga, S.; Lamberti, C.; Zecchina, A. *Prog. Surf. Sci.* **2004**, *76*, 71.

(3) Klingshirn, C. *Phys. Status Solidi B* **2007**, *244*, 3027.

(4) Woell, C. *Prog. Surf. Sci.* **2007**, *82*, 55.

(5) Djurisic, A. B.; Leung, Y. H. *Small* **2006**, *2*, 944.

(6) Takeuchi, I.; Yang, W.; Chang, K. S.; Aronova, M. A.; Venkatesan, T.; Vispute, R. D.; Bendersky, L. A. *J. Appl. Phys.* **2003**, *94*, 7336.

(7) Lin, S. S.; Hong, J. I.; Song, J. H.; Zhu, Y.; He, H. P.; Xu, Z.; Wei, Y. G.; Ding, Y.; Snyder, R. L.; Wang, Z. L. *Nano Lett.* **2009**, *9*, 3877.

(8) Ozgur, U.; Alivov, Y. I.; Liu, C.; Teke, A.; Reshchikov, M. A.; Dogan, S.; Avrutin, V.; Cho, S. J.; Morkoc, H. *J. Appl. Phys.* **2005**, 98.

(9) Bates, C. H.; Roy, R.; White, W. B. *Science* **1962**, *137*, 993.

(10) Segnit, E. R.; Holland, A. E. *J. Am. Ceram. Soc.* **1965**, *48*, 409.

(11) Eijt, S. W. H.; de Roode, J.; Schut, H.; Kooi, B. J.; De Hosson, J. T. M. *Appl. Phys. Lett.* **2007**, 91.

(12) Lu, G.; Lieberwirth, I.; Wegner, G. *J. Am. Chem. Soc.* **2006**, *128*, 15445.

(13) Chen, J.; Shen, W. Z.; Chen, N. B.; Qiu, D. J.; Wu, H. Z. *J. Phys.: Condens. Matter* **2003**, *15*, L475.

(14) Stankic, S.; Sternig, A.; Finocchi, F.; Bernardi, J.; Diwald, O. *Nanotechnology* **2010**, *21*, 355603.

(15) Sternig, A.; Klacar, S.; Bernardi, J.; Stoeger-Pollach, M.; Gronbeck, H.; Diwald, O. *J. Phys. Chem. C* **2011**, *115*, 15853.

(16) Müller, R.; Mädler, L.; Pratsinis, S. E. *Chem. Eng. Sci.* **2003**, *58*, 1969.

(17) Tani, T.; Watanabe, N.; Takatori, K.; Pratsinis, S. E. *J. Am. Ceram. Soc.* **2003**, *86*, 898.

(18) Tani, T.; Mädler, L.; Pratsinis, S. E. *J. Nanopart. Res.* **2002**, *4*, 337.

(19) Samerjai, T.; Liewhiran, C.; Phanichphant, S. *Advanced Materials and Nanotechnology: Proceedings of the International Conference (AMN-4)*; Dunedin, New Zealand, Feb 8−12, 2009 ; Hendy, S. C.; Brown, I. W. M., Eds.; American Institute of Physics: College Park, MD, 2009; p 17.

(20) Mädler, L.; Roessler, A.; Pratsinis, S. E.; Sahm, T.; Gurlo, A.; Barsan, N.; Weimar, U. *Sens. Actuators, B* **2006**, *114*, 283.

(21) Stoklosa, A.; Laskowska, B. *J. Chem. Crystallogr.* **2008**, *38*, 913.

(22) Ohtomo, A.; Kawasaki, M.; Koida, T.; Masubuchi, K.; Koinuma, H.; Sakurai, Y.; Yoshida, Y.; Yasuda, T.; Segawa, Y. *Appl. Phys. Lett.* **1998**, *72*, 2466.

(23) Kim, Y.-I.; Page, K.; Seshadri, R. *Appl. Phys. Lett.* **2007**, 90.

(24) Choopun, S.; Vispute, R. D.; Yang, W.; Sharma, R. P.; Venkatesan, T.; Shen, H. *Appl. Phys. Lett.* **2002**, *80*, 1529.

(25) Park, W. I.; Yi, G. C.; Jang, H. M. *Appl. Phys. Lett.* **2001**, *79*, 2022.

(26) Wang, Y. S.; Thomas, P. J.; O'Brien, P. *J. Phys. Chem. B* **2006**, *110*, 21412.

(27) Stankic, S.; Muller, M.; Diwald, O.; Sterrer, M.; Knozinger, E.; Bernardi, J. *Angew. Chem., Int. Ed.* **2005**, *44*, 4917.

(28) Stankic, S.; Cottura, M; Demaille, D; Noguera, C; Jupille, J. *J. Cryst. Growth* **2011**, *329*, 52.

(29) Mueller, M.; Stankic, S.; Diwald, O.; Knoezinger, E.; Sushko, P. V.; Trevisanutto, P. E.; Shluger, A. L. *J. Am. Chem. Soc.* **2007**, *129*, 12491.

(30) Diwald, O.; Sterrer, M.; Knözinger, E. *Phys. Chem. Chem. Phys.* **2002**, *4*, 2811.

(31) Stankic, S.; Bernardi, J.; Diwald, O.; Knözinger, E. *J. Phys. Chem. B* **2006**, *110*, 13866.

(32) van Dijken, A.; Meulenkamp, E. A.; Vanmaekelbergh, D.; Meijerink, A. *J. Lumin.* **2000**, *90*, 123.

(33) Vanmaekelbergh, D.; van Vugt, L. K. *Nanoscale* **2011**, *3*, 2783.

(34) John, T. T.; Priolkar, K. R.; Bessiere, A.; Sarode, P. R.; Viana, B. *J. Phys. Chem. C* **2011**, *115*, 18070.

■ NOTE ADDED AFTER ASAP PUBLICATION

This paper was published on the Web on May 3, 2012. Additional corrections were added throughout the paper, and the corrected version was reposted on May 8, 2012.